Stimulated Cherenkov emission in dielectric-lined waveguides

W. Peter
Department of Physics, Ben-Gurion University, Beersheva, Israel

E. Garate
Department of Physics, University of California, Irvine, California 92717
(Received 12 December 1991)

Particle-in-cell simulations of a dielectric Cherenkov maser experiment are used to analyze the emissive characteristics of an annular relativistic beam in a dielectric-lined waveguide. Good agreement with recent experimental results is obtained. The large gain in the device follows linear theory until saturation, when particle bunching and trapping is observed. The beam density becomes highly modulated with pulse length $\sim\lambda/2$, where λ is the guide wavelength. The performance of the device in the high-current regime is highly nonlinear. A simple nonlinear theory, confirmed by numerical results, shows that the field saturates at a value corresponding to $\omega_b=\Delta\omega/2$, where ω_b is the electron bounce frequency in the wave and $\Delta\omega$ is the detuning parameter.

PACS number(s): 41.75.Fr, 41.60.Cr, 52.25.Sw, 42.52.+x

I. INTRODUCTION

Stimulated Cherenkov emission from a relativistic electron beam in a slow wave structure is a source of coherent high-power microwave radiation [1–5]. In this configuration, the electron beam can interact with the subluminous waveguide mode to enable the Cherenkov instability to grow (Fig. 1). A requirement for this is that the electron distribution function have a positive derivative, i.e., $\partial f/\partial v>0$ near the phase velocity $v\simeq v_{\rm ph}$ of the wave. This assures a population inversion, or more electrons in a "higher" energy state than in a "lower" one, which then guarantees the prevalence of stimulated emission over absorption. Hence there is a net production of radiative photons, and the resonant wave-particle interaction at the Cherenkov condition $\omega=\mathbf{k}\cdot\mathbf{v}$ causes the beam (which has most of its energy in the axial direction) to bunch.

In Fig. 2 is shown a schematic drawing of a high-power dielectric Cherenkov maser experiment whose details have been previously published [6]. The device consists of an annular electron beam traveling down a dielectric-lined waveguide through which a 100-kW input signal is injected at the entrance to the drift tube. The liner had a dielectric constant $\epsilon=10$, outer radius of 1.75 cm, and was inserted into a thin-walled stainless-steel drift tube. The inner radius of the tapered liner varied between 1.47 and 1.5 cm, and liner lengths of up to 30 cm were used. A Physics International Pulserad 220A was used to energize the electron-beam diode. Beam voltages of between 500 kV and 1 MV were generated with interaction currents up to 5 kA at a pulse duration of 100 ns. The electron beam was annular with a thickness $\sim$2 mm. Magnetic guide fields of up to 20 kG were used to guide the electron beam through the dielectric liner at a distance of $\sim$ 2 mm from the liner surface. A tunable magnetron (8.4–9.0 GHz) was used to supply an input signal of up to 100 kW. Figure 2 is a schematic of the experimental apparatus. Depending on the liner and beam parameters, output powers of up to 280 MW at 11% efficiency were measured. The experiment was studied in the parameter regimes corresponding to three distinct configurations which are summarized in Table I.

In [7] we presented results on the comparisons of a $2\frac{1}{2}$-dimensional, fully electromagnetic, and relativistic particle-in-cell code ISIS [8] with the experimental measurements of Ref. [6]. In this study, we discuss the nature of the beam-wave interaction and analyze a number of simulations detailing the nature of the particle-wave coupling in the waveguide. The simulations are based on the experimental configuration of Ref. [6] with a simulation region of 60 cm length, a 59-cm liner length, and a constant liner thickness of $\sim$0.24 cm. The liner length used in the simulations was larger than that used in the experiments in order to investigate the length over which saturation of the interaction occurred.

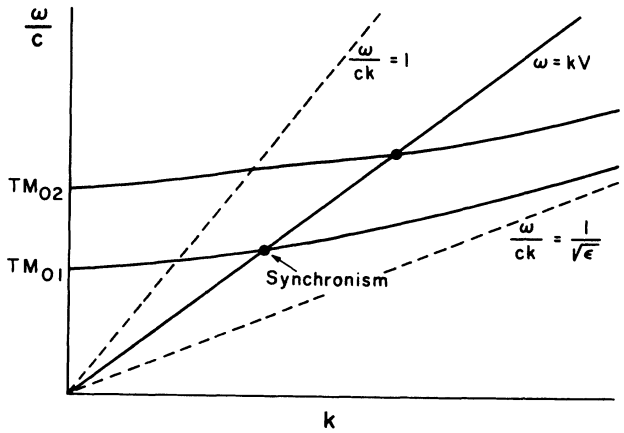

FIG. 1. Plot of the intersection of the no-beam waveguide dispersion relation with the beam line $\omega=k\beta c$ near where the Cherenkov resonance occurs.

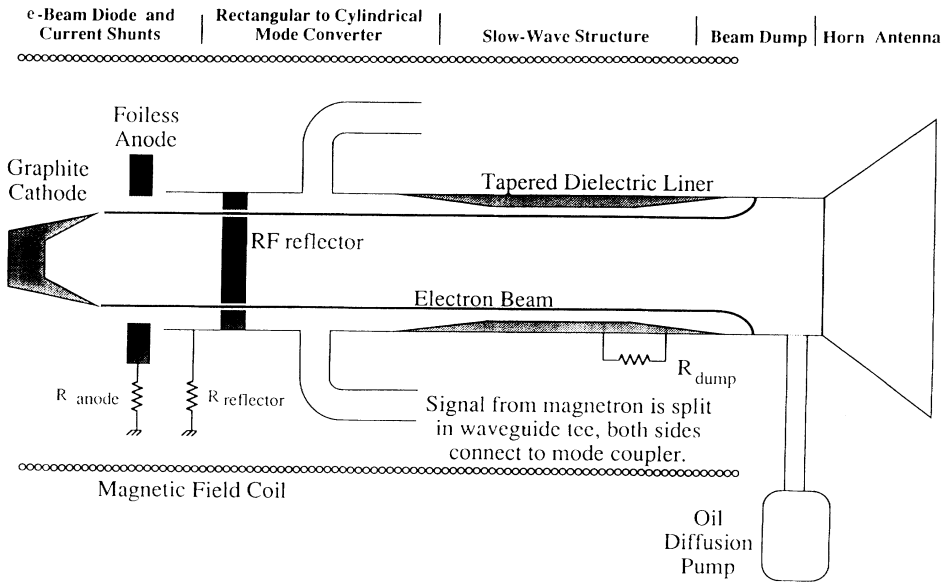

FIG. 2. Schematic drawing of the dielectric Cherenkov maser amplifier experiment of Ref. [1] (not to scale).

II. SIMULATIONS

In a typical simulation, a relativistic electron beam with an energy varying between 788 and 890 keV and with an energy spread $\Delta\gamma/\gamma_0$ between 1.7% and 12% was injected into a metallic drift tube of radius 1.75 cm and axial length 60 cm. In all the simulations there was a constant magnetic guide field of magnitude $B_z = 15$ kG applied in the z direction. A TM_{01} wave of power 100 kW was launched into the left-hand side ($z=0$) of the drift tube with a frequency that could be varied. The beam current was ramped up smoothly to its asymptotic value over ~ 1 ns. This helped prevent large amplitude noise from occurring at the input to the waveguide. The same was done for the input rf power.

The primary set of simulations was based on the 8.6-GHz, 788-kV, 3.1-kA electron-beam configuration (case B of Table I). The input power of 100 kW was carefully benchmarked in the code by simulating an empty waveguide with no beam present. A typical particle plot of the device at a time of approximately 7 ns is shown in Fig. 3. Note the strong particle bunching beginning at a position of $z \sim 30$ cm. The bunch length of each electron pulse is ~ 1.8 cm, close to the value of a half wavelength in the empty waveguide $\lambda/2 = 1.75$, and approximately equal to the half wavelength in the guide determined from the linear dispersion relation (see below), $\lambda/2 = 1.36$. This suggests particle trapping in the wave troughs.

The simulations were based on typical beam energy spreads of $\Delta\gamma/\gamma \sim 1.7\%$, which is an exaggerated upper limit for cold field-emission cathodes which typically have less than $\Delta\gamma/\gamma_0 \sim 0.5\%$ at these currents and beam voltages [9]. A set of simulations with variable $\Delta\gamma/\gamma$ were run to investigate the effect of beam energy spread on gain. For example, for the parameters of case A, it was found that the gain was decreased by 8.2% when the beam energy spread was increased to $\Delta\gamma/\gamma_0 \sim 3.0\%$.

The dispersion relation for this configuration is given by [5]

TABLE I. Summary of the parameters for the three experimental configurations of the dielectric Cherenkov maser [6].

	Case A (low-current short liner)	Case B (high-current medium liner)	Case C (low-current long liner)
Input frequency (GHz)	8.9	8.6	8.9
Liner thickness (cm)	0.27	0.27	0.24
Liner length (cm)	17.8	23.9	30
Taper length (cm)	6.4	3.3	15
Beam voltage (kV)	890	788	800
Beam current (kA)	0.5	3.1	1.3

$$\frac{T}{p}\left[\frac{TI_0(u)\{I_1(x)K_1(v)-K_1(x)I_1(v)\}+I_1(u)\{I_0(v)K_1(x)+K_0(v)I_1(x)\}}{-TI_0(u)\{K_0(x)I_1(v)+K_1(v)I_0(x)\}+I_1(u)\{K_0(x)I_0(v)-I_0(x)K_0(v)\}}\right]=-\frac{\epsilon}{q}\frac{J_1(qb)Y_0(qd)-Y_1(qb)J_1(qd)}{J_0(qb)Y_0(qd)-Y_0(qb)J_0(qd)}\ , \tag{1}$$

where J_n and Y_n are Bessel and Neumann functions of order n, and I_n and K_n are the corresponding modified Bessel functions. In the above equation we have defined $p=(k^2-\omega^2/c^2)^{1/2}$, $q=(\omega^2\epsilon/c^2-k^2)^{1/2}$, $u=pa$, $x=pTa$, $v=pTb$, and the quantity T is given in terms of the beam plasma frequency $\omega_p^2=(4\pi n_0 e^2/\gamma_0^3 m)$ by

$$T=\left[1-\frac{\omega_p^2}{(\omega-kv)^2}\right]^{1/2}. \tag{2}$$

As schematically drawn in Fig. 4, a is the electron-beam inner radius, and b and d are the dielectric liner inner and outer radii, respectively. In the derivation of the dispersion relation no gap is assumed between the outer radius of the annular electron beam and the inner dielectric surface. Because interest is in an amplifier configuration (i.e., a convective instability), the dispersion relation is solved for $k=k(\omega)$ with real ω. For an input frequency of 8.6 GHz, the dispersion relation yields $k_r=\mathrm{Re}\{k\}=2.3$ and $\gamma_k=\mathrm{Im}\{k\}=0.145$.

A number of simulations of this configuration were conducted with the magnetron frequency used as an adjustable parameter. The linear gain $\mathrm{Im}\{k\}$ for each run was calculated by taking the average of a number of measurements at different times for $t>5$ ns. In Fig. 5 is plotted $\mathrm{Im}\{k\}$ from the dispersion relation versus frequency for a current of 1.3 kA. It is seen that the simulations agree very well with the linear gain curve derived from Eq. (1).

In the course of the experiments, an output power signal was measured even when no input was supplied by the magnetron. This was due to impedance mismatches at the end of the waveguide and to the high gain of the interaction. The effect of this feedback phenomenon on the experiment was to make the voltage pulse length the equivalent of about 30 passes through the dielectric liner region.

A simulation was performed to investigate the possibility of high gain in the experiment with no input power. The results indicate that even though significant gain did occur, peak fields at the same times were an order of magnitude less than the case for when the magnetron was turned on. In addition, the frequency spectrum of the power was broad and not locked into the particular frequency of the power source. This can be seen in Fig. 6, where a comparison between the experimental results and simulations is presented. Note that in the absence of input power, the physics in the device is initially dominated by spontaneous Cherenkov emission processes. Some of this spontaneously emitted radiation will interact with beam particles downstream to produce some stimulated emission, but since this is proportional to the wave intensity, the output power is significantly less. The cause of the distinct dip in the power spectrum near 8.4 GHz in both the experiment and simulation results is unknown.

Figure 7 is a plot of the gain versus injected beam current for a series of simulations at a frequency 8.6 GHz. The fitted curve to the simulation data $\propto I^{0.289}$ is in between the high-gain "strong-pump" regime $\propto I^{1/3}$

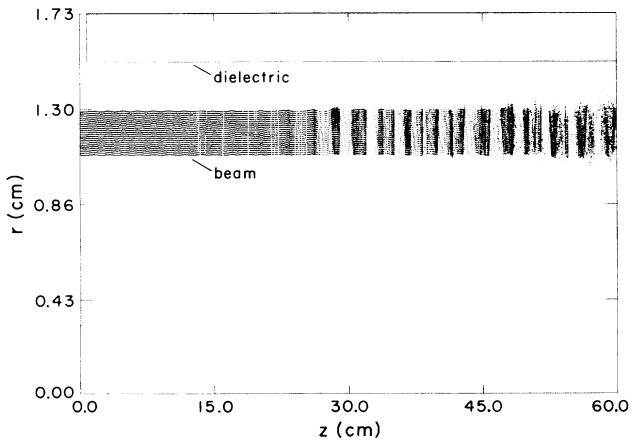

FIG. 3. Particle snapshot r vs z at a time $t\sim 6$ ns. A significant amount of beam bunching is seen in the 3.1-kA electron beam (case B).

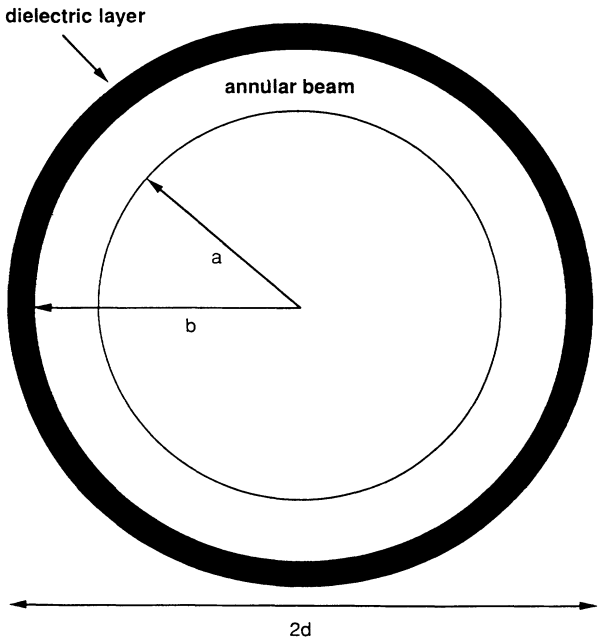

FIG. 4. Schematic drawing in radial geometry illustrating the quantities used to derive the dispersion relation in the text. The wall radius is d, and the dielectric inner and outer radii are b and c, respectively.

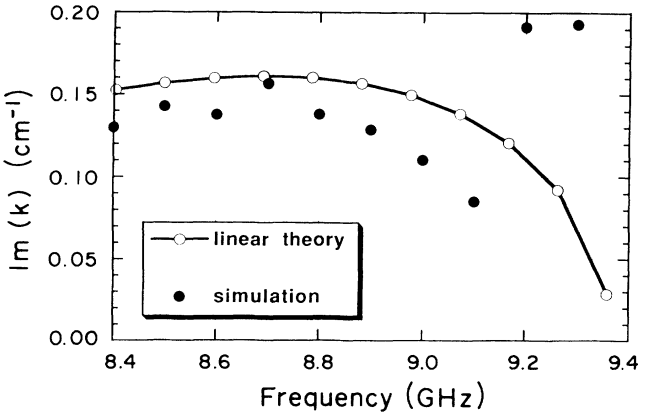

FIG. 5. Plot of linear gain $\mathrm{Im}\{k\}$ vs frequency for simulations for the low-current case as compared with solutions to the dispersion relation Eq. (1).

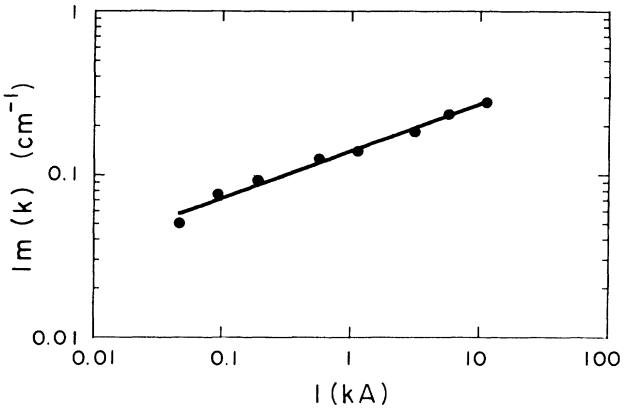

FIG. 7. Plot of $\mathrm{Im}\{k\}$ vs injected beam current at a frequency of 8.6 GHz. The fitted curve to the simulation data is $\propto I^{0.289}$, in between the high-gain "strong-pump" regime ($\propto I^{1/3}$) and the high-gain collective (i.e., Raman) regime ($\propto I^{1/4}$).

[2,10,11] and the high-gain collective (i.e., Raman) regime $\propto I^{1/4}$ [11,12]. It should be mentioned that the simulation results were a sensitive function of the liner thickness, as can be easily verified from linear theory. Zoning in the radial direction therefore had to be as fine as possible (within financial constraints of supercomputer time) in order to resolve the required thickness. In addition, note that the linear calculations do not take into account

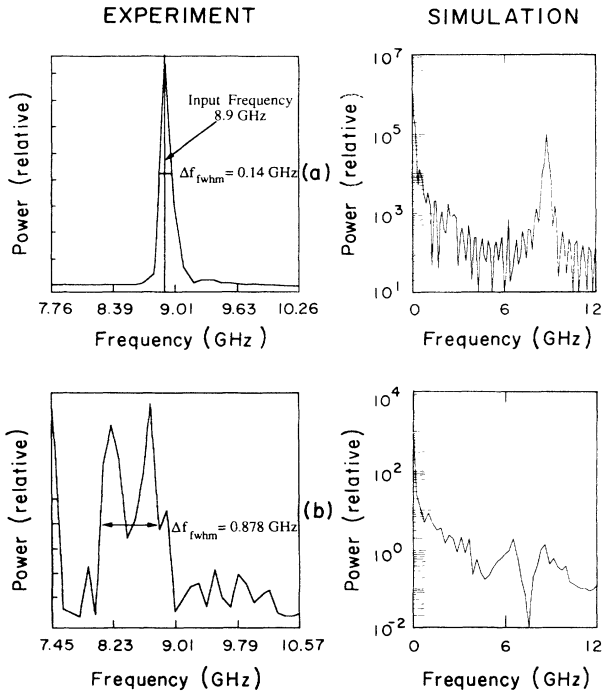

FIG. 6. Emission spectrum of experiment (left) and simulation (right) for the low-current 8.9-GHz case. The top results are with an input signal and the bottom results are with the magnetron turned off. Note the distinct dip near 8.4 GHz in the power spectrum with no input power for both the experiment and simulation.

space-charge depression of the beam or multimode effects while the simulations do.

Power output was measured directly in the simulation, as in the experiment, by dumping the beam before the exit to the waveguide and measuring the rf power at the exit. In case B a peak output power of over 900 MW was observed at the simulated waveguide exit for a peak efficiency of 37% and a gain of 37.8 dB, equivalent to $\mathrm{Im}\{k\}=0.18\ \mathrm{cm}^{-1}$. This agrees with the high-end efficiency estimates of a number of authors [12,13], and in particular with the 600-MW, 32% efficiency, and linear gain $\mathrm{Im}\{k\}=0.18\ \mathrm{cm}^{-1}$ analysis of Freund [14]. These theoretical results can be compared with the experimental traces which show a peak power output of 280 MW and an efficiency of 11%. The difference between experiment and theory has been attributed to dielectric breakdown [7]. In case C a power of 130 MW was observed in the simulations for an efficiency of 12.5% and a gain of 33.6 dB. In the experiment, peak power output was given at 90 MW for an 8.6% efficiency. A summary of the output power in both the simulations and the experiment is presented in Table II.

In Fig. 8 we show a "phase" space plot showing particle energy $(\gamma-1)mc^2$ as a function of axial position downstream from the drift tube entrance. The plot is made for the high-current 3.1-kA, 8.6-GHz case. It is evident how the initial monoenergetic beam with energy $(\gamma_0-1)mc^2$ is modified by the wave-particle interaction. More electrons have lost energy ($\gamma<\gamma_0$) than have gained energy ($\gamma>\gamma_0$), indicating wave growth and a gain in radiative power. Note the presence of a coherent particle clump, probably corresponding to those particles trapped in the bottom of the wave potential [15,16]. The clump seems to oscillate between essentially zero energy and the incident particle energy. After some distance, there appears to be a loss of coherence of the clump with an associated increase in the amount of phase mixing. A complete rotation of the clump in phase space seems to occur

TABLE II. Comparison between experimental and simulation results for the high-power amplifier.

	Case A		Case B		Case C	
	Expt.	Simul.	Expt.	Simul.	Expt.	Simul.
Output power (MW)	13	12–13	280	900	90	130
Efficiency (%)	3	3	13	37	8.6	12.5

over a 20-cm distance down the drift tube. Such phase space rotations are usually the cause of amplitude oscillations in the electric field. This has been observed in the simulations, as will be discussed later.

In Fig. 9, a phase space plot showing electron momentum $\gamma\beta_z$ versus z is shown for the low-current, 8.9-GHz case at a time of 4 ns. After saturation, the minimum energy of the particle distribution is seen to steadily increase, suggesting that the particles are now steadily taking energy away from the wave [13]. That this is so is demonstrated by a plot of the axial electric field near the dielectric liner E_z versus z (Fig. 10) for the same configuration at the same time.

Another plot of the axial electric field at the liner surface as a function of distance is shown in Fig. 11 for the high-power 8.6-GHz case. The electric field is plotted using a logarithmic scale to show the large gain associated with the device, though the negative half cycles of the field are flipped to make them positive in the logarithmic plot. As can be seen, the field saturates at around $z=30$ cm and reaches a peak value of 200 kV/cm. Note the good agreement with linear theory which predicts field growth $\propto e^{\gamma_k z}$, where $\gamma_k=\mathrm{Im}\{k\}$ is a constant. The value of γ_k is easily calculated from Fig. 11 to be 0.18 cm^{-1}, which compares with the value obtained from the linear dispersion relation, $\mathrm{Im}\{k\}=0.145\ \mathrm{cm}^{-1}$. The wave does not grow indefinitely but will saturate in the cold beam limit by particle trapping in the troughs of the wave.

It is usually desirable to maximize the power output from a given device by terminating the interaction region at an appropriate length L such that the emitted power is maximum. Note that the logarithmic scale in Fig. 11 has flipped the negative half cycles of E_z to positive values so that the slow modulation which appears to have a wavelength of 10 cm in Fig. 11 has actually doubled the wavelength, $\lambda\simeq 20$ cm. The fast electric-field oscillation at the input frequency ($\lambda\simeq 3.5$ cm) and the slow modulation at $\lambda\simeq 20$ cm makes the determination of an appropriate resonator length L more difficult than a steady-state model [13] might predict.

The decrease in electric field after saturation in the low-current 1.3-kA case may be related to the experimental configuration. In this case, the predicted gain from linear theory was quite low, and the power gain from the simulation agreed with the experiment only when feedback effects of the wave from the downstream boundary were taken into account. In the simulations, saturation was not seen until many light transit times across the simulation region, indicating that the feedback in the simulation caused this configuration to act like a frequency-locked oscillator and not an amplifier, in agreement with experiment. When feedback and wave reflection effects are taken into account, Bogdankevich, Kuzelev, and Rukhadze [13] showed that the electric field in a Cherenkov resonator reaches a maximum at saturation and then monotonically decreases, as shown in Fig. 10. As is seen in Fig. 11, this decrease in electric field after saturation was not always evident in the high-power case.

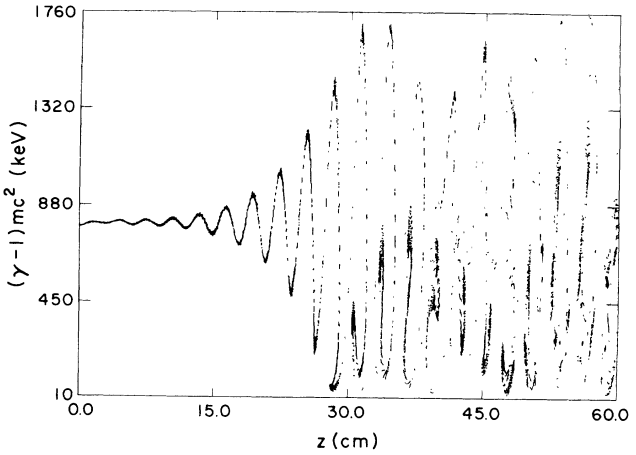

FIG. 8. "Phase space" plot of particle energy $(\gamma-1)mc^2$ vs axial distance z in the high-power 8.6-GHz, 3.1-kA case. Note the presence of a relatively coherent electron clump which oscillates between essentially zero energy and the beam injection energy as it travels down the drift tube. The clump appears to perform a complete rotation in phase space over a 20-cm length down the drift tube, corresponding to the 20-cm slow modulation wavelength seen in Fig. 11. Phase mixing near the end of the drift tube is easily seen in the figure.

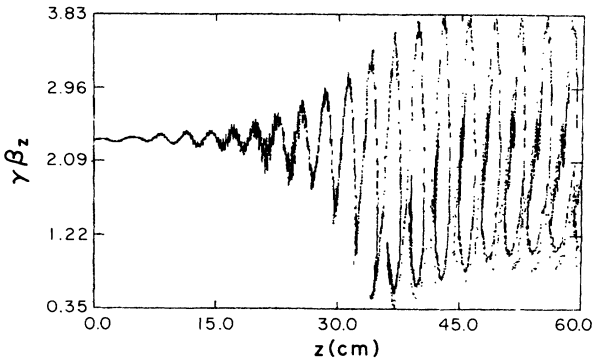

FIG. 9. Phase space plot of particle momentum $\gamma\beta_z$ vs axial distance z in the low-power 8.9-GHz case. The phase rotation of a relatively coherent particle clump is also seen in this figure, albeit with an oscillation wavelength ($\sim$ 30 cm) larger than that seen in Fig. 8. The snapshot is taken at 4 ns.

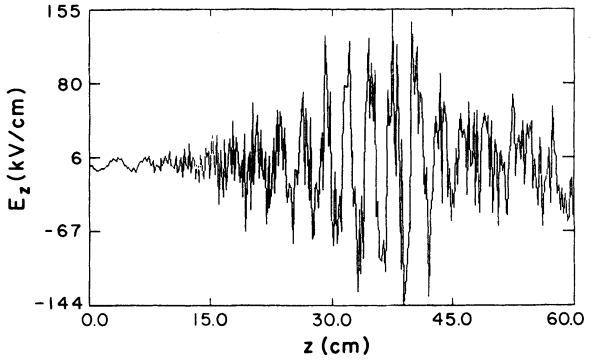

FIG. 10. Plot of the axial electric field E_z near the dielectric liner as a function of distance along the waveguide. The snapshot corresponds to the same configuration and time as Fig. 9.

III. DISCUSSION AND CONCLUSIONS

The low-frequency modulation in the electric field E_z seen in Fig. 11 appears to be due to the phase rotation of trapped particles in the electric-field troughs. As electrons travel back and forth in the rf well, the electron axial velocity oscillates about zero, and there is continuous exchange of energy between the wave and the beam. Conservation of energy requires that when electrons acquire their maximum velocity, the wave is at its minimum amplitude. If the liner length had been long enough, the 20-cm oscillations in amplitude seen in Fig. 11 might have been seen to damp out due to phase mixing. This situation is usually described in an oscillator configuration by a time-dependent growth rate $\gamma_k=\gamma_k(t)$ [15] or in an amplifier configuration by a spatial growth rate $\Gamma_k=\gamma_k/(\partial\omega/\partial k)=\mathrm{Im}\{k\}$ [17]. In the limit of linear growth, the quantity γ_k (or Γ_k) is constant. As the

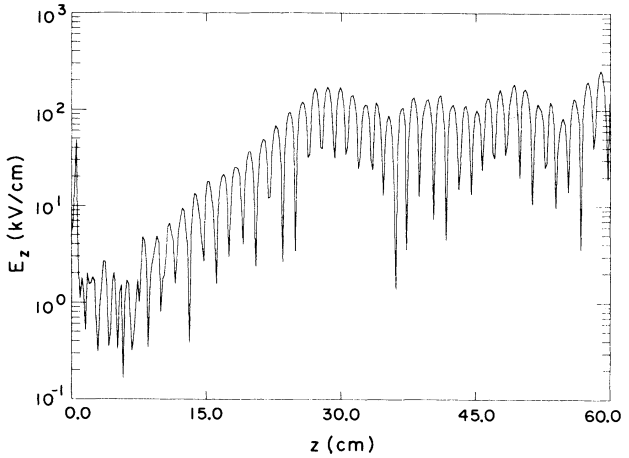

FIG. 11. Plot of the axial electric field E_z as a function of distance along the waveguide at a time of 7 ns for the high-current 3.1-kA configuration. A logarithmic scale is used for E_z to show the increase in gain (over two orders of magnitude in 30 cm) more clearly, but cannot reproduce the negative values of E_z (cf. Fig. 9). The large spike in E_z near $z=0$ is due to the untapered dielectric liner (cf. Fig. 3).

electric field grows, the particles are trapped in the growing amplitude of the wave and the field saturates at a given value. The field amplitude then oscillates about this value with damped oscillations corresponding to a "bounce" frequency which is the oscillation frequency of an electron at the bottom of the ponderomotive well [15].

Consider an electron in an infinitely strong axial guide field satisfying the usual force equation

$$\frac{d}{dt}(\gamma\beta_z)=\frac{e}{mc}E_z \ . \tag{3}$$

Note that this equation can also be written in the form

$$\frac{d\gamma}{dt}=\dot{\gamma}=\frac{e}{mc}\beta_z E_z \ , \tag{4}$$

which explicitly describes the nature of the interaction, i.e., if $\dot{\gamma}>0$ the particle takes energy from the field and if $\dot{\gamma}<0$ the particle loses energy to the field. From Fig. 11, it is seen that the electric field oscillates with an increasing amplitude $E_0(z)$ until particles are trapped in the potential well, and growth ceases. From Fig. 11, the electric field before saturation is seen to vary as

$$E_z(z,t)=\mathcal{E}_0(z)\cos(kz-\omega t+\phi) \ , \tag{5}$$

where ϕ is the phase angle. The amplitude $\mathcal{E}_0(z)\sim\exp(\gamma_k z)$, where $\gamma_k=\mathrm{Im}\{k\}$ is the growth rate. After saturation the amplitude can be taken to be constant, $\mathcal{E}_0=E_0\exp(\gamma_k z_s)$, where z_s is the saturation length.

Note the zero-order solution to Eq. (3) is given by $z(t)=z_0+\beta_0 ct$, where β_0 is the injection velocity. As the wave amplitude increases, this electron motion is modified and to first order

$$z(t)=z_0+\beta_0 ct+\delta z(t) \ , \tag{6}$$

where $\delta z(t)$ describes deviations from the zero-field solution and satisfies $\dot{\delta z}(t)/c\ll\gamma_0^{-2}$ [19]. Define $k=k_r+i\gamma_k$ and a modified axial variable by $\zeta(t)=\zeta_0+\Delta\omega t+k_r\delta z(t)$, where $\zeta_0=\zeta(0)=k_r z_0+\phi-\pi/2$. The detuning parameter $\Delta\omega=\beta_0 kc-\omega$ is essentially the relative velocity between the electrons and the wave phase velocity, i.e., $\Delta\omega=k\Delta v$, where $\Delta v=\beta_0 c-\omega/k$. When this parameter is greater than zero, the electrons can give energy to the wave; when the parameter is less than zero, the wave can give energy to the electrons. When $\Delta\omega=0$, the electrons are "on resonance" and no energy exchange (and hence gain) takes place. With these definitions, Eqs. (3) and (5) then become

$$\ddot{\zeta}(t)=-\omega_b^2\sin\zeta(t) \tag{7}$$

which is the classical pendulum equation having elliptic integral solutions. For small $\zeta(t)$, $\sin\zeta(t)\approx\zeta(t)$, the equation is a simple harmonic oscillator equation with frequency determined by the so-called bounce frequency

$$\omega_b^2=\left[\frac{eE_0k}{\gamma_0^3 m}\right] \tag{8}$$

and describes trapped particle motion in a potential trough. It is essentially the frequency for which the ki-

netic energy of electrons moving at the phase velocity of the wave is as large as the wave potential. For the input parameters of the high-power 8.6-GHz case, and the resultant peak electric field at 200 kV/cm from Fig. 11, we have $\omega_b \sim 7\times 10^9$. The first integral of Eq. (7) is

$$[\dot{\zeta}(t)]^2 = 2\omega_b^2[\cos\zeta(t) - \cos\zeta_0] + (\Delta\omega)^2 . \quad (9)$$

It is evident from Eq. (9) that the strength of the interaction corresponds to the quantity $\omega_b^2/(\Delta\omega)^2$. If this quantity is small, the particles move essentially according to the zero-order solutions; if this quantity is large Eq. (9) describes closed phase space paths for some electrons. As the electric field grows and $\omega_b^2/(\Delta\omega)^2 \gg 1$, all electrons can be considered to be "on resonance," i.e., the increased energy in the fields has been obtained at the expense of electron kinetic energy. The electrons are then slowed down so that eventually $\Delta\omega \rightarrow 0$ and gain ceases.

Colson [19] solved Eq. (3) in the limit of small $\omega_b^2/(\Delta\omega)^2$ for use in a classical free-electron laser configuration. In this approximation, the particle positions can be written to second order as

$$z(t) = z_0(t) + \beta_0 ct + \frac{\omega_b^2 c}{\Delta\omega^2}[\sin(\Delta\omega t + \zeta_0) - \sin\zeta_0 - \Delta\omega t\cos\zeta_0] . \quad (10)$$

The second-order corrections are evidently periodic in ζ_0 and are responsible for the spatial bunching. Half of the electrons within a given $\lambda_r = 2\pi/k_r$ are accelerated by the wave and half of the electrons are decelerated. There is then a "split" in the energy distribution function [19], as has been verified in numerical simulations of the nonlinear saturation of the electron cyclotron maser [21]. The fourth-order terms have the effect of widening and skewing the distribution such that for positive values of the detuning parameter, there is a net gain in the energy of the radiation field.

Note that the expansion of Eq. (9) in the small parameter $(\omega_b/\Delta\omega)^2$ breaks down for large enough values of the radiation field. This is just saturation of the field, and is equivalent to the case for which the detuning parameter $\Delta\omega = 0$. In such a case, the electron has given up its "excess" energy to the field, and now finds itself "on resonance."

It is possible to get a clearer understanding of the physics of field saturation and particle trapping in the single-wave model by considering the solutions to Eq. (9) more exactly. It is easy to show from the elliptic integral solutions [22] to Eq. (8) that the character of the solutions changes dramatically from trapped particle orbits in phase space to untrapped orbits when

$$(\Delta\omega)^2 = 2\omega_b^2(1+\cos\zeta_0) . \quad (11)$$

The electric field will grow until all the available free energy is depleted. For a given value of the detuning parameter, Eq. (11) predicts that any particle with a given initial ζ_0 will be trapped if the electric field satisfies $\omega_b^2 = (\Delta\omega)^2/4$ or

$$\omega_b = (\Delta\omega)/2 . \quad (12)$$

For the parameters of the high-power 8.6-GHz case, $\Delta\omega = 9.62$. Hence a peak value of the electric field of 186 kV/cm is obtained, which compares with the value of 200 kV/cm obtained from the simulations, as can be seen in Fig. 11.

The condition $\omega_b = \Delta\omega/2$ is equivalent to the same condition usually written as

$$\Delta\omega = 4eE_0 k/m \quad (13)$$

for the nonlinear saturation of the two-stream instability [23]. The correspondence between the nonlinear evolution of the Cherenkov instability and the two-stream instability has been suggested before [12]. The saturation condition, Eq. (13), is interpreted as the minimum value of electric field required to trap electrons moving at a relative velocity $\Delta v = k\Delta\omega$ with respect to the wave. (This neglects the effect of electron velocity modulation on the trapping process.) The spatial bunching can be easily derived in this model. Linearizing the continuity equation,

$$\frac{\partial n}{\partial t} + \frac{\partial}{\partial z}(nv_z) = 0 \quad (14)$$

with respect to the velocity $v = v_0 + v_1$ and density $n = n_0 + n_1$ [where the first-order quantities are assumed to vary as $\exp i(kz - \omega t)$], one obtains

$$\frac{n_1}{n_0} = -\frac{v_1}{\Delta v} . \quad (15)$$

From Eq. (15) it is evident that one will have $n_1 \sim n_0$, (i.e., the beam density modulation equal to the beam density itself) when $v_1 \sim \Delta v$. When does v_1 become comparable to Δv? As in the derivation leading to Eq. (7), we can linearize the equation of motion Eq. (3) to give

$$\frac{v_1}{v_0} = \frac{e}{\gamma_0^3 m}\frac{\phi_1}{v_0\Delta v} , \quad (16)$$

where $\phi_1 \sim E_0/k$ is the electric potential. From this equation, one finds that $v_1 \sim \Delta v$ when

$$(\Delta v)^2 \sim \frac{eE_0}{\gamma_0^3 mk} \quad (17)$$

or, equivalently, $\omega_b \sim \Delta\omega$, which is essentially the condition given in Eq. (11) apart from a numerical factor. Hence the saturation requirement $\omega_b \sim \Delta\omega/2$ can also be viewed as a condition for 100% density modulation of the beam. This interpretation correlates nicely with the significant particle bunching seen in Fig. 3 after field saturation.

The applicability of the single-wave model, described by Eqs. (3) and (5), is usually valid as long as the bandwidth of growing waves is narrow enough to allow consideration of only the fastest growing mode [16,23]. In an amplifier configuration, this should be valid for interaction lengths not much larger than a few "bounce" lengths $(2\pi v_{ph}/\omega_b)$ after saturation. Beyond this interaction length, it would be possible for neighboring waves within the main bandwidth of the principal mode to grow in amplitude enough to affect the beam dynamics. In cases where the configuration behaved like a frequency-locked

oscillator, the single-wave model should be valid for a few e-folding times after trapping [16].

Consider, for example, particle distribution plots $N(\epsilon)$ versus ϵ in Fig. 12 where $\epsilon=(\gamma-1)mc^2$ is the electron energy. The data are taken from the low-current 1.3-kA simulation at a time $t\simeq 5.5$ ns. The sharp peak at the injection energy of 890 keV ($\gamma_0=2.74$) is easily seen. Note that this distribution plot includes all particles within the simulation region, including those just having entered and just about to leave. Figure 12(b) is a distribution plot at a later time of $t\simeq 8$ ns. The peak is now reduced by 36% and a secondary peak at a slightly lower energy becomes noticeable. This is indicative of quasilinear diffusion, and not of single-wave models [19]. At a time of 8 ns, the configuration (which behaved more like an oscillator than an amplifier) had enough time for the fastest growing mode to saturate, and for the particles to trap. Hence neighboring waves (that is, waves within a small bandwidth of the main wave) at this time have undoubtedly become as large as the fastest growing wave and the nonlinear beam dynamics must now be treated by the usual multiwave methods of quasilinear theory.

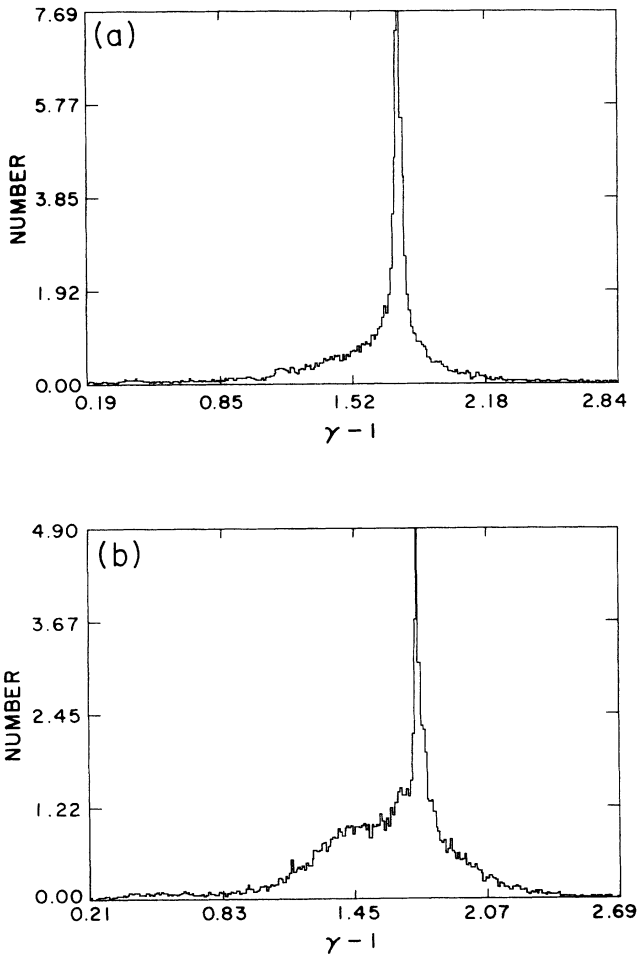

FIG. 12. (a) Energy distribution plot $N(\epsilon)$ vs $\epsilon=(\gamma-1)mc^2$ for a simulation of the case A configuration at a time $t\simeq 5.5$ ns. The particle distribution is peaked around the injected energy at 890 keV. (b) A similar plot at a time of $t\simeq 8$ ns showing the diffusion of higher-energy electrons into a large number of lower-energy states.

Finally, we will discuss the expected characteristic oscillation length in electric field E_z and the ~20-cm modulation seen in Fig. 11 after saturation. The observed oscillation wavelength should be many times the magnitude of L, where $L=\omega_b/(\omega/k)$ is related to the electron bounce frequency ω_b in the bottom of the potential well [15,18]. For the high-power experiment L is ~3.3 cm, which is consistent with the observed 20-cm wavelength in Fig. 11. In the high-power experiment we have $\gamma_k L\sim 0.6$, so that the observed oscillation wavelength is an even larger multiple of L that would be expected from linear theory [15,17]. In this parameter range, the electric-field amplitude can no longer be considered constant, and the trapping of initially untrapped electrons must be included. A more quantitative comparison between the slow modulations seen in Fig. 11 and theory would require detailed numerical calculations and involve consideration of other effects (e.g., finite geometry).

In conclusion, particle-in-cell simulations for several configurations of a high-power dielectric Cherenkov maser suggest that strong wave-particle interaction is observed in the device. A simple nonlinear theory can be used to provide estimates of the electric-field magnitude at saturation, and better understanding of the trapping dynamics. The simulations underscore the fact that the physics of the Cherenkov maser is similar to that of the free-electron laser [11,19,20] and cyclotron maser [21]. However, it has the advantages of relative simplicity of operation, and robustness in handling relatively large beam thermal spreads [14,24].

Referring to Fig. 3, significant particle bunching in the high-current case can be seen during the interaction. Results of the simulation indicate that the beam current can be 90% modulated. Power probes indicate approximately 0.8 GW of power in the bunched beam, which represents ~33% of the total beam power. Such a bunched beam could be used to drive an output cavity as in the relativistic klystron [25], or by exploiting ~50-ns pulses to amplify input signals for short time scales where breakdown might not be a problem. Given the high efficiency of power extraction for these type devices, gigawatt power levels could be attained. Alternatively, the bunched beam could be used to drive a high-gradient (> 100 MV/m) accelerator in a relatively compact device [26].

ACKNOWLEDGMENTS

The authors are grateful to A. Gover, M. Gedalin, C. M. Snell, W. Main, and D. S. Lemons for discussions and to R. Prohaska for technical help. This research was supported in part by the Academic Computing Office of the University of California, Irvine, through an allocation of computing resources. Partial support from the Israel Ministry of Science is also gratefully acknowledged. Supercomputer calculations were supported by a grant from the San Diego Supercomputer Center which is funded by the National Science Foundation.

[1] A. N. Didenko, A. R. Borisov, G. P. Fomenko, and Yu. G. Shtein, Pis'ma Zh. Tekh. Fiz. **9**, 60 (1983) [Sov. Tech. Phys. Lett. **9**, 26 (1983)].
[2] J. Walsh, T. Marshall, and S. Schlesinger, Phys. Fluids **20**, 709 (1977).
[3] E. Garate and J. Walsh, IEEE Trans. Plasma Sci. **PS-13**, (1985).
[4] W. Main, R. Cherry, and E. Garate, Appl. Phys. Lett. **55**, 1498 (1989).
[5] W. Main, R. Cherry, and E. Garate, IEEE Trans. Plasma Sci. **PS-18**, 507 (1990).
[6] E. Garate, H. Kosai, W. Peter, A. Fisher, W. Main, J. Weatherall, and R. Cherry, in Microwave and Particle Beam Sources and Directed Energy Concepts, edited by Howard E. Brandt [Proc. SPIE **1226**, 238 (1990)].
[7] W. Peter, E. Garate, W. Main, and A. Fisher, Phys. Rev. Lett. **65**, 2989 (1990).
[8] G. Gisler, M. E. Jones, and C. M. Snell, Bull. Am. Phys. Soc. **29**, 1208 (1984).
[9] S. C. Chen and T. C. Marshall, Phys. Rev. Lett. **52**, 425 (1984).
[10] W. Case, in *High Power Microwave Sources,* edited by V. L. Granatstein and I. Alexeff (Artech, Boston, 1987), p. 397.
[11] A. Gover and P. Sprangle, IEEE J. Quantum Electron. **QE-17**, 1196 (1981).
[12] D. S. Lemons and L. E. Thode, Phys. Rev. Lett. **56**, 2684 (1986).
[13] L. S. Bogdankevich, M. V. Kuzelev, and A. A. Rukhadze, Usp. Fiz. Nauk **133**, 3 (1981) [Sov. Phys. Usp. **24**, 1 (1981)].
[14] H. P. Freund, Phys. Rev. Lett. **65**, 2989 (1990).
[15] T. M. O'Neil, Phys. Fluids **8**, 2255 (1965).
[16] T. M. O'Neil, J. H. Malmberg, and J. H. Winfrey, Phys. Fluids **14**, 1204 (1971); T. M. O'Neil and J. H. Winfrey, *ibid.* **15**, 1514 (1972).
[17] L. H. Oei and D. G. Swanson, Phys. Fluids **15**, 2218 (1972).
[18] A. Lee and G. Schmidt, Phys. Fluids **13**, 2546 (1970).
[19] W. B. Colson, in *Novel Sources of Coherent Radiation,* edited by S. F. Jacobs, M. Sargent III, and M. O. Scully (Addison-Wesley, Reading, MA, 1978), p. 157.
[20] N. M. Kroll, P. L. Morton, and M. N. Rosenbluth, IEEE J. Quantum Electron. **QE-17**, 1436 (1981).
[21] P. Sprangle and A. T. Drobot, IEEE Trans. Microwave Theory Tech. **MTT-25**, 528 (1977).
[22] See, for example, J. J. Stoker, *Nonlinear Vibrations in Mechanical and Electrical Systems* (Interscience, New York, 1950), p. 25.
[23] W. E. Drummond, J. H. Malmberg, T. M. O'Neil, and J. R. Thompson, Phys. Fluids **13**, 2422 (1970).
[24] T. H. Kho and A. T. Lin, IEEE Trans. Plasma Sci. **18**, 513 (1990).
[25] M. Friedman and V. Serlin, Rev. Sci. Instrum. **58**, 1 (1987).
[26] M. Friedman, V. Serlin, Y. Y. Lau, and J. Krall, Phys. Rev. Lett. **63**, 2468 (1989).

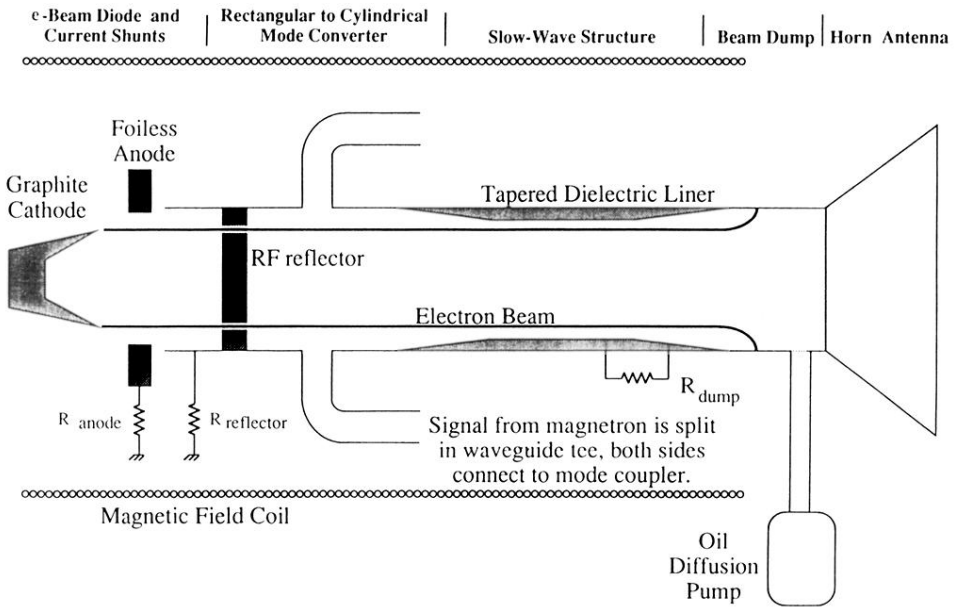

FIG. 2. Schematic drawing of the dielectric Cherenkov maser amplifier experiment of Ref. [1] (not to scale).